

Matching-Based Few-Shot Semantic Segmentation Models Are Interpretable by Design

Pasquale De Marinis^{1,*} Uzay Kaymak^{2,3} Rogier Brussee² Gennaro Vessio¹ Giovanna Castellano¹

¹ Department of Computer Science, University of Bari Aldo Moro

² Jheronimus Academy of Data Science (JADS)

³ Eindhoven University of Technology (TU/e)

{pasquale.demarinis, gennaro.vessio, giovanna.castellano}@uniba.it,

u.kaymak@ieee.org, r.brussee@jads.nl

Abstract

Few-Shot Semantic Segmentation (FSS) models achieve strong performance in segmenting novel classes with minimal labeled examples, yet their decision-making processes remain largely opaque. While explainable AI has advanced significantly in standard computer vision tasks, interpretability in FSS remains virtually unexplored despite its critical importance for understanding model behavior and guiding support set selection in data-scarce scenarios. This paper introduces the first dedicated method for interpreting matching-based FSS models by leveraging their inherent structural properties. Our Affinity Explainer approach extracts attribution maps that highlight which pixels in support images contribute most to query segmentation predictions, using matching scores computed between support and query features at multiple feature levels. We extend standard interpretability evaluation metrics to the FSS domain and propose additional metrics to better capture the practical utility of explanations in few-shot scenarios. Comprehensive experiments on FSS benchmark datasets, using different models, demonstrate that our Affinity Explainer significantly outperforms adapted standard attribution methods. Qualitative analysis reveals that our explanations provide structured, coherent attention patterns that align with model architectures and enable effective model diagnosis. This work establishes the foundation for interpretable FSS research, enabling better model understanding and diagnostic for more reliable few-shot segmentation systems. The source code is publicly available at <https://github.com/pasqualedem/AffinityExplainer>.

1. Introduction

Deep learning has achieved remarkable performance in areas such as image recognition [23], speech processing [14], and language translation [51]. However, the internal reasoning of deep models remains opaque due to their high complexity and large parameterization, making them “black boxes” [27]. This lack of transparency poses challenges in domains requiring accountability, such as healthcare and law.

Explainable AI (XAI) aims to address this issue, and significant progress has been made for conventional tasks like image classification and language modeling. Yet, explainability in Few-Shot Learning (FSL) remains underexplored. FSL seeks to generalize from a handful of labeled examples per class, addressing data scarcity and cost constraints [47]. Despite its practical importance, most FSL studies focus on accuracy rather than interpretability.

This lack of attention is even more pronounced in the subdomain of *Few-Shot Semantic Segmentation* (FSS), where existing models are primarily evaluated based on accuracy without addressing how or why specific segmentation outputs are produced. In FSS, the choice of the few labeled samples (support images) is crucial, as they provide the model with the necessary context to segment objects in the query image. When a model fails to produce a satisfactory output, it is often unclear whether the issue lies in the model’s architecture, the choice of support images, or the inherent difficulty of the task. This ambiguity highlights the importance of interpretability in FSS models, as it enables the “diagnosis” of model failures and enhances performance by informing the selection of suitable support images.

In particular, *matching-based* FSS models [17, 22, 33, 52, 55], which operate by computing similarity between support and query image features, offer a potential avenue for explainability due to their inherent matching mechanism. However, to date, there is no dedicated work that

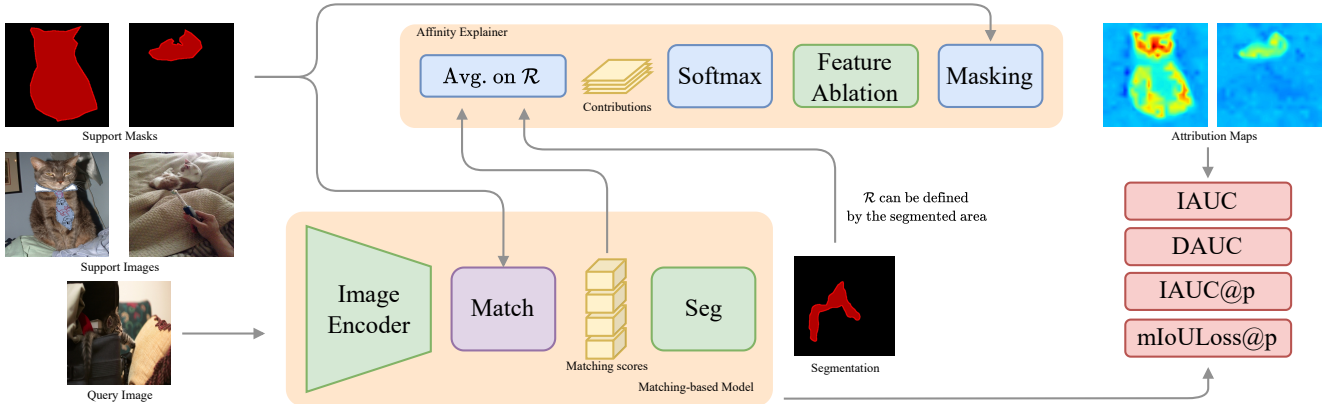


Figure 1. Illustration of the proposed framework with two examples and one class. The Affinity Explainer method can be applied to any matching-based FSS model adhering to the illustrated structure. It computes attribution maps using the matching scores between query and support images. Attribution is restricted to a region \mathcal{R} —typically defined by the ground truth mask, segmentation output, or user-specified input. These maps are then softmax-normalized, weighted via feature ablation, and aggregated to yield the final attribution map. The resulting maps highlight the support image regions most influential in segmenting the query, thereby enabling model interpretability. Evaluation is performed using the proposed metrics.

explicitly leverages this matching mechanism to interpret model predictions.

This study addresses the limited interpretability of matching-based Few-Shot Semantic Segmentation models by introducing *Affinity Explainer* (AffEx), a framework comprising three variants that directly build on the core matching mechanisms underlying these models. Starting from the raw similarity scores computed between query and support features, AffEx derives contribution maps, which are then aggregated via feature ablation to produce attribution heatmaps over the support set. These heatmaps reveal the specific support pixels that most strongly influence the segmentation of the query image, providing actionable insights into how support information is utilized during inference. The three variants—Unmasked, Masked, and Signed AffEx—differ in how the support masks are incorporated into the attribution process, offering complementary perspectives on model behavior. Affinity Explainer is model-agnostic and can be applied to any matching-based FSS architecture. The broader goal is to connect the methodological design of FSS models with the principles of explainable AI (XAI), establishing a foundation for future research in interpretable few-shot segmentation. The overall framework is illustrated in Fig. 1.

The contributions of this paper are as follows.

- We introduce a novel method for interpreting matching-based FSS models, leveraging the inherent structure of their matching operations to provide insights into model predictions.
- We extend the concept of Insertion Area Under the Curve and Deletion Area Under the Curve to the FSS domain, providing a framework for evaluating the interpretability

of segmentation outputs.

- We provide a benchmark of several explainability methods on popular FSS models and datasets, demonstrating the effectiveness of our proposed approach.

2. Related Work

2.1. Few-Shot Semantic Segmentation

FSS integrates the principles of semantic segmentation with those of FSL, addressing scenarios where annotated data is limited [10, 37, 41, 43]. Semantic segmentation assigns a class label to each pixel in an image, but conventional models require large annotated datasets, which are often impractical to obtain. FSL alleviates this issue by learning from only a few labeled examples per class [47].

In an N -way K -shot episode, the model receives a support set $\mathcal{S} = \{(\mathbf{I}_i, \mathbf{M}_i)\}_{i=1}^{N \times K}$ of K annotated examples per class and a query image I_q that may contain up to N target classes. The objective is to predict the corresponding segmentation masks $\hat{\mathbf{M}}_q = f_\theta(I_q, \mathcal{S})$, where f_θ denotes the segmentation model parameterized by θ . Performance is typically averaged over multiple episodes sampled from disjoint class sets to evaluate generalization to unseen categories.

Early FSS approaches relied on prototype learning, where prototypes are formed via masked average pooling and compared to query features [5, 7, 46, 50, 54]. Despite their efficiency, these methods reduce spatially structured features to single vectors, leading to a loss of fine-grained spatial information [18, 52]. To address this, some works introduce multiple prototypes per class [20, 49]. In contrast, matching-based methods [6, 17, 22, 33, 52, 55] com-

pute dense correspondences between support and query images at the pixel level. This preserves spatial granularity and improves performance on segmentation tasks. However, the dense affinity computation incurs higher computational costs, limiting scalability in practical applications.

Despite growing interest in FSS, the field continues to emphasize accuracy at the expense of interpretability. The internal mechanisms by which FSS models arrive at their outputs remain largely unexamined, indicating a significant research gap in explainable few-shot segmentation.

2.2. Explainability in Few-Shot Learning

Interpretability in computer vision is often pursued through relevance heatmaps, which can be class-specific or class-agnostic. Key explainability categories include saliency-based methods [56], activation-based approaches via forward or backward passes [8, 53], perturbation techniques [11], and game-theoretic models like Shapley values [21].

Attribution methods offer theoretical grounding: Deep Taylor Decomposition [24] distributes relevance scores recursively while preserving their sum. Layer-wise Relevance Propagation (LRP) [3] and its variants [25] generally operate in a class-agnostic manner [13], though class-specific versions exist [12]. Gradient-based methods, including SmoothGrad [36], FullGrad [38], and Grad-CAM [31], analyze input gradients or deep features to provide explanations, with Grad-CAM being class-specific. Nonetheless, their application to FSL remains sparse and under-evaluated.

Some FSL methods embed interpretability directly into their design [19, 44, 45], while others adapt model-agnostic explainers such as LIME and SHAP [1, 30]. These approaches often yield partial explanations confined to specific modules, such as the feature extractor, overlooking inter-module interactions. A separate line of work employs surrogate models—e.g., autoencoders trained on the same data—to generate architecture-independent explanations [42], though this introduces dataset dependence and limits generalization.

Few studies compare FSL-specific interpretability methods with standard model-agnostic tools, likely due to the challenges posed by episodic training and data sparsity [39]. As a result, the field lacks a consistent framework for evaluating interpretability in FSL, and the empirical reliability of existing methods remains underexplored. Moreover, model-agnostic explainers face inherent difficulties in FSL settings involving joint support-query processing or multimodal inputs. For instance, [9] had to modify a Siamese network’s prediction function to integrate LIME, revealing structural incompatibilities between such explainers and FSL models.

To our knowledge, no prior work has addressed interpretability in few-shot segmentation. This paper addresses

this gap by leveraging the inherent matching mechanisms of FSS models to generate interpretable segmentation outputs. By grounding interpretability in the structural design of FSS, we aim to advance XAI in the few-shot domain.

3. Method

3.1. Matching-Based FSS Models

Matching-based Few-Shot Semantic Segmentation models operate by comparing features extracted from support and query images to produce segmentation masks. These models typically consist of three main components: a feature extractor or image encoder F , a matching mechanism $Match$, and a segmentation head Seg . The feature extractor, often a convolutional neural network or a vision transformer, processes both the support and query images to produce high-dimensional feature maps. The matching mechanism then computes similarities, also referred to as matching scores, between the features of the support images and those of the query image, typically using distance metrics such as cosine similarity or Euclidean distance. Finally, the segmentation head generates the final segmentation mask based on the computed similarities. Given a support set \mathcal{S} of k image-mask pairs for class c , the model predicts a mask \hat{M}_q for a query image I_q as

$$\begin{aligned} \hat{M}_q &= f_\theta(I_q, \mathcal{S}) \\ &= \text{Seg}_\theta(\text{Match}_\theta(F_\theta(I_q), F_\theta(I_{\mathcal{S}}), M_{\mathcal{S}})), \end{aligned} \quad (1)$$

where F_θ is the feature extractor, Match_θ the matching mechanism, and Seg_θ the segmentation head, all parameterized by θ . The overall pipeline corresponding to this formulation is illustrated in the *Matching-based Model* block of Fig. 1.

Given an image I , the feature extractor produces a feature map $F_\theta(I) \in \mathbb{R}^{C \times H \times W}$ where C is the number of channels and H and W are the height and width of the feature map, respectively. However, several works have shown that using mid-level features can also improve the performance of FSS models [4, 28, 33]. Therefore, we define the feature extractor as a function that returns a set of feature maps:

$$F_\theta(I) = \{F_\theta^1(I), F_\theta^2(I), \dots, F_\theta^n(I)\}, \quad (2)$$

where $F_\theta^j(I) \in \mathbb{R}^{C_j \times H_j \times W_j}$ denotes the j -th feature map with C_j channels and spatial dimensions $H_j \times W_j$.

The matching module can be decomposed into three components: (i) an input mapping module $\text{Map}_\theta^{\text{in}}$, which transforms the features and masks into a common relational space (including normalization, reshaping, or non-linear projections such as those used in attention mechanisms); (ii) a matching mechanism MM_θ (e.g., cross-attention or Euclidean distance) that computes the matching scores between support and query representations; and (iii) an output

mapping module $\text{Map}_\theta^{\text{out}}$ that aggregates the matching results to produce a single feature map.

The matching mechanism can be summarized as

$$P_S = \text{Map}_\theta^{\text{in}}(F_\theta(I_S), M_S) \quad (3)$$

$$P_q = \text{Map}_\theta^{\text{in}}(F_\theta(I_q)) \quad (4)$$

$$\Sigma = \left\{ \sigma^j = \text{MM}_\theta(P_q^j, P_S^j) \right\}_{j=1}^n \quad (5)$$

$$F_{\text{out}} = \text{Map}_\theta^{\text{out}}(\Sigma), \quad (6)$$

where P_S is the mapped support set, P_q is the mapped query image, Σ is the matching score set, and F_{out} is the output feature map. The segmentation head then processes the output feature map to produce the final segmentation mask:

$$\hat{M}_q = \text{Seg}_\theta(F_{\text{out}}). \quad (7)$$

3.2. Interpreting Matching-Based FSS Models

To interpret matching-based FSS models, we propose Affinity Explainer (AffEx)—a method that leverages the inherent structure of matching operations. The key idea is to analyze the contributions of individual support images to the final segmentation mask by examining the matching scores and their corresponding feature maps. This approach allows us to identify which support images and features are most influential in determining the segmentation output for a given query image. This relies on the assumption that the matching scores reflect the relevance of each support image to the query image.

Let $\mathcal{S} = \{(I_i, M_i)\}_{i=1}^K$ be the support set with images and corresponding masks. Let $I_q \in \mathbb{R}^{C \times H_q \times W_q}$ be the query image, and (x, y) a pixel location in I_q . We define an attribution function

$$\mathcal{A} : (I_q, (x, y), \mathcal{S}) \mapsto \mathbb{R}^{K \times H_s \times W_s} \quad (8)$$

which returns, for a given query pixel, a spatial attribution map for each support image. The attribution value at pixel (x, y) of support image I_i is denoted

$$\alpha_{i,x,y} = [\mathcal{A}(I_q, (x, y), \mathcal{S})]_{i,x,y} \quad (9)$$

and quantifies the contribution of that pixel to the segmentation prediction at (x, y) in the query. Let $\mathcal{R} \subseteq [1, H_q] \times [1, W_q]$ be a region of interest in the query image I_q . We extend the attribution function \mathcal{A} to operate over \mathcal{R} by computing the mean attribution across all pixels in \mathcal{R} :

$$\mathcal{A}(I_q, \mathcal{R}, \mathcal{S}) := \frac{1}{|\mathcal{R}|} \sum_{(x,y) \in \mathcal{R}} \mathcal{A}(I_q, (x, y), \mathcal{S}). \quad (10)$$

The attribution function \mathcal{A} can also be extended to operate over the feature maps of the images: $\mathcal{A}(F_{\theta_q}, \mathcal{R}, F_{\theta_S})$.

We assume that the attribution of a pixel in the support image to the query image can be approximated by the attribution of the corresponding pixel in the feature map and in the mapped feature map: $\alpha_{i,x,y} \approx \mathcal{A}(F_{\theta_q}, (u, v), F_{\theta_S}) \approx \mathcal{A}(P_q, (u, v), P_S)$, where $(u, v) = \phi(x, y)$ are the pixel coordinates in the feature map corresponding to image coordinates (x, y) , accounting for the spatial downsampling introduced by F_θ and expressed through ϕ .

Let $\sigma^j \in \mathbb{R}^{H_j \times W_j \times K \times H_j \times W_j}$ be the matching scores for the mapped query feature map $P_q^j(I_q)$ and the mapped support feature maps $P_S^j(\mathcal{S})$ at the layer j coming from Eq. (5). These scores serve as the input to the proposed method, illustrated in the *Affinity Explainer* block of Fig. 1. The attribution function for an element (u, v) in the query feature map can be defined as

$$\mathcal{A}(P_q^j, (u, v), P_S^j) = \text{softmax}(\sigma_{u,v}^j) \in \mathbb{R}^{K \times H_j \times W_j} \quad (11)$$

where P_q^j and P_S^j are the mapped feature maps for the query and support images at layer j , respectively. The softmax function normalizes scores and maps them to a probability distribution.

At this step, we have a set of attribution maps for each layer j in the feature extractor, which can be aggregated to obtain a single attribution map for the query image. The aggregation can be done by a weighted summation of the attribution maps across all layers:

$$\mathcal{A}(I_q, (u, v), \mathcal{S}) = \sum_{j=1}^n w_j \cdot \mathcal{A}(P_q^j, (u, v), P_S^j) \quad (12)$$

where w_j are the weights assigned to each layer. The weights are calculated based on the importance of each layer in the matching process. This is determined through *feature ablation*, a technique in which individual features or components are systematically removed to evaluate their contribution to the overall performance:

$$w_j = \frac{|f_{\theta, \text{head}}(\Sigma) - f_{\theta, \text{head}}(\Sigma_{-j})|}{\sum_{k=1}^n |f_{\theta, \text{head}}(\Sigma) - f_{\theta, \text{head}}(\Sigma_{-k})|}, \quad (13)$$

where $f_{\theta, \text{head}}(\cdot) = \text{Seg}_\theta(\text{Map}_\theta^{\text{out}}(\cdot))$, Σ_{-k} is the set of matching scores obtained by replacing the feature map at layer k with a zero tensor of the same shape, effectively removing the contribution of that layer to the matching process.

The attributions computed at this stage can already be used to generate attribution maps, as they capture the information conveyed by the support set; we refer to this variant as *Unmasked AffEx*. To further refine the results, we incorporate the support masks by applying them to the support features before computing the matching scores, thereby constraining the attributions to the regions defined by the masks. To avoid sharp transitions at mask boundaries, a

Gaussian smoothing is applied to the masks prior to masking the features, resulting in the *Masked AffEx* variant. Finally, instead of discarding background regions, we interpret them as having a negative contribution to the model’s prediction by assigning a value of -1 to the background area of the support masks before weighting. This yields the *Signed AffEx* variant.

3.3. Causal Evaluation Metrics

To evaluate the interpretability of the segmentation outputs, we extend the concepts of the two causal metrics Insertion Area Under the Curve (IAUC) and Deletion Area Under the Curve (DAUC) [29] to the FSS domain. These metrics are designed to quantify the decision perturbation in the model when changing the image according to the explanation.

Defined for classification, these metrics gradually perturb/de-perturb the inputs. To extend them in the FSS scenario, we perturb the support set while leaving the query image unchanged, since our attribution task is based on the support set given the query image.

Given a support set $\mathcal{S} = \{(I_i, M_i)\}_{i=1}^K$ and a query image I_q , we define the Deletion Area Under the Curve as follows:

$$\text{DAUC}(I_q, \mathcal{S}, \mathcal{A}_{\mathcal{R}}) = \sum_{t \in \mathcal{T}} f_{\theta}(I_q, \mathcal{P}(\mathcal{S}, \Gamma_t(\mathcal{A}_{\mathcal{R}}))), \quad (14)$$

where \mathcal{T} is a discrete set of perturbation steps (e.g., fractions of perturbed pixels), $\mathcal{P}(\mathcal{S}, \Gamma_t(\mathcal{A}))$ is the perturbed support set obtained by perturbing the top t pixels according to the attribution map $\mathcal{A}_{\mathcal{R}} = \mathcal{A}(I_q, \mathcal{R}, \mathcal{S})$ in the region of interest \mathcal{R} , and f_{θ} is the segmentation model. The selection function Γ_t selects the top t pixels coordinates from the attribution map \mathcal{A} based on their values, i.e., $\Gamma_t(\mathcal{A}) = \{(u, v) \in [1, H_s] \times [1, W_s] : \alpha_{u,v} \in \text{top}_t(\mathcal{A})\}$.

The logic behind DAUC is that if the attribution map is accurate, perturbing the support set by removing the most relevant pixels should decrease the model’s confidence in the segmentation prediction. Therefore, DAUC measures the extent to which the model’s confidence decreases when the most relevant pixels are removed from the support set. On the other hand, the Insertion Area Under the Curve, starting from a completely perturbed support set, measures how much the model’s confidence increases when the most relevant pixels are added to the support set and thus is defined correspondingly. To compute the AUC metrics, we need to define the region over which the confidence scores will be evaluated. In this work, we use the region of the predicted mask $\mathcal{R}_{\hat{M}_q}$ as the evaluation area.

Since model confidence is often uncalibrated and highly model-dependent, we also propose a variant in which the IAUC and DAUC metrics are evaluated using the mIoU instead of the model’s confidence. We refer to these variants as $\text{IAUC}_{\text{Conf}}$ ($\text{DAUC}_{\text{Conf}}$) and $\text{IAUC}_{\text{mIoU}}$ ($\text{DAUC}_{\text{mIoU}}$), respectively.

We also define two additional metrics. $\text{IAUC}_{\text{Conf}@p}$ represents the $\text{IAUC}_{\text{Conf}}$ calculated by considering only a percentage p of the most relevant pixels. In the FSS scenario, the model can successfully segment the image even when only a small percentage of the most relevant pixels is considered. Therefore, the most significant aspect of the IAUC is the initial portion of the curve. The second metric is $\text{mIoULoss}@p$, which quantifies the accuracy loss incurred by the models when using the most relevant pixels, as determined by the explanation method, compared to the complete support set:

$$\hat{M}_{fl} = f_{\theta}(I_q, \mathcal{S}) \quad (15)$$

$$\hat{M}_{pt} = f_{\theta}(I_q, \mathcal{P}(\mathcal{S}, \Gamma_p(\mathcal{A}))) \quad (16)$$

$$\text{mIoULoss}@p = \text{mIoU}_M(\hat{M}_{fl}) - \text{mIoU}_M(\hat{M}_{pt}), \quad (17)$$

where $\text{mIoU}_M(\cdot)$ is the mean Intersection over Union (mIoU) calculated between the predicted mask and the ground truth mask M . $\text{mIoU}_M(\hat{M}_{pt})$ is the mIoU of the query image with respect to the perturbed support set obtained by perturbing the top percentage p pixels according to the attribution map $\mathcal{A}_{\mathcal{R}} = \mathcal{A}(I_q, \mathcal{R}, \mathcal{S})$ in the region of interest \mathcal{R} . Unlike $\text{IAUC}_{\text{Conf}@p}$ —which relies on model confidence scores—this metric decouples evaluation from the model’s confidence bias, enabling a more direct assessment of the explanation method’s utility in terms of segmentation performance.

4. Experiments

We evaluate two representative matching-based models: DCAMA [33] and DMTNet [4]. Their interpretability is assessed using the proposed attribution framework and the causal evaluation metrics $\text{DAUC}_{\text{mIoU}}$, $\text{IAUC}_{\text{mIoU}}$, their difference, $\text{IAUC}_{\text{Conf}@0.01}$, and $\text{mIoULoss}@p$ with $p \in \{0.01, 0.05\}$. We compare these results against several well-established attribution methods applicable to few-shot segmentation: Saliency Maps [35], Integrated Gradients [40], Guided Integrated Gradients [16], XRAI [15], Blur IG [48], Deep Lift [34], and LIME [30]. It is important to note that methods such as Grad-CAM [31] are not directly applicable to few-shot segmentation models. These approaches rely on feature activations from a specific convolutional layer, producing attribution maps with spatial dimensions tied to that layer’s output rather than to the support set. As a result, they cannot generate attributions that align spatially with the support images, making them unsuitable for this setting. Also, some methods like Guided IG cannot be applied to specific models (e.g., DMTNet) due to architectural constraints.

In addition to the several established attribution techniques applicable to FSS models, we introduce two simple yet informative baselines. First, a *random* explanation baseline provides a reference point by producing attribution

maps entirely independent of the model: it generates a tensor with the same shape as the attribution map, with values sampled uniformly from $[0, 1]$. Second, since FSS models inherently focus on the region defined by the support mask, we define a naive mask-based baseline that leverages this prior directly. Specifically, this baseline returns a slightly perturbed version of the support mask as the explanation. We refer to it as the *Gaussian Noise Mask*, computed as $\mathcal{A}_{\mathcal{R}} = M_s + \epsilon$, where $\epsilon \sim \mathcal{N}(0, \sigma^2)$ and $\sigma = 0.01$. This produces a soft attribution map that reflects the model’s spatial prior without relying on learned features.

We evaluated both models on two widely used FSS datasets: COCO 20ⁱ [26] and Pascal 5ⁱ [32]. All experiments are performed on a single NVIDIA A100.

4.1. Quantitative Evaluation

Table 1 reports the interpretability evaluation results on COCO 20ⁱ and Pascal 5ⁱ for DCAMA and DMTNet under the 1-way 5-shot setting. Note that the $\text{IAUC}_{\text{mIoU}}$ and $\text{DAUC}_{\text{mIoU}}$ values vary across models—even for the random baseline—as they reflect each model’s intrinsic performance. This indicates that IAUC and DAUC, taken individually, are not directly comparable across models. To obtain a more meaningful assessment, we therefore compute the difference $\text{IAUC} - \text{DAUC}$ for each explanation method and model. This difference quantifies the asymmetry in the relevance of regions that contribute positively ($\text{IAUC}_{\text{mIoU}}$) and negatively ($\text{DAUC}_{\text{mIoU}}$) to the model’s prediction. A higher value indicates that the explanation method better concentrates confidence on semantically relevant regions, whereas values close to zero or negative suggest weak or misleading explanations.

From the results, considering the difference metric, we observe that the simple Gaussian Noise Mask serves as a surprisingly strong baseline, outperforming or matching most competing methods. This finding highlights the need for explanation techniques specifically tailored to the FSS setting. In some cases, even the Unmasked AffEx variant fails to surpass this baseline, emphasizing the importance of incorporating support-mask information into the attribution process. Moreover, the masked variants only slightly improve over the baseline, suggesting that focusing attention solely on the support-mask area already introduces a strong prior into the model’s decision-making.

To verify that AffEx not only attends to the correct region but also assigns meaningful pixel-wise importance, we examine the fine-grained metrics computed at specific perturbation thresholds ($@p$). These metrics emphasize the initial, most influential pixels, thus amplifying differences between explanation methods. In particular, the $\text{mIoULoss}@p$ results clearly show that the AffEx variants outperform all other methods, confirming their ability to accurately rank the support pixels that most contribute to the correct seg-

mentation of the query image.

Under the 1-shot setting (Tab. 2), we observe similar trends. However, as fewer pixels are available in the support set, the interpretability performance of all methods decreases accordingly.

We also conducted a computational cost analysis. AffEx runs substantially faster than gradient-based baselines (182 ms vs. 2.6–13 s on DCAMA; 427 ms vs. 5–17 s on DMTNet) and uses moderate memory (about 3.3 GB and 2.4 GB in the 1-shot setting), far below the most demanding methods (e.g., DeepLift up to 13 GB). Full results are provided in the supplementary material.

4.2. Qualitative Evaluation

Figure 2 presents qualitative interpretability results for Saliency, Blur IG, XRAI, and the different AffEx variants applied to the DMTNet and DCAMA models spanning four representative episodes.

Across all episodes, we observe clear qualitative differences in the heatmaps generated by the various methods. Gradient-based approaches such as Saliency and Blur IG tend to produce noisier and less localized attributions. XRAI, which relies on region-based aggregation, yields more coherent but still relatively diffuse heatmaps compared to AffEx. In contrast, the AffEx variants generate more structured and sharply focused visual explanations. Moreover, AffEx shows greater model dependence, as its attributions directly reflect the internal feature representations of the underlying network. For instance, DMTNet (first two rows) produces importance maps that align with object-level semantics, whereas DCAMA (last two rows) highlights distinct regions within the same object, revealing differing attention patterns.

In the first episode, we observe an incorrect segmentation. This example highlights one of the key advantages of the proposed framework: analyzing the factors that drive the model to segment certain regions instead of others. All methods exhibit a strong correlation with the support mask area, as expected. However, only Unmasked AffEx and Signed AffEx also capture the sink region, providing valuable insight into what misled the model’s decision.

The second episode illustrates how semantically related but visually distinct entities (motorcycle and motorcyclist) exhibit substantial similarity, significantly influencing the model’s prediction. This suggests that models heavily relying on the foreground–background distinction of the support mask can be misled in such cases. A similar phenomenon is observed in the third episode, where the model associates the baseball bat with the glove.

The fourth episode shows how different parts of the same object can have different levels of importance in the segmentation process. In this case, the AffEx variants highlight the horse’s tail as the most important region. More

Model	Dataset	COCO 20 ⁱ						Pascal 5 ⁱ					
		Explanation Method	IAUC mIoU	DAUC mIoU	Diff.	IAUC Conf @0.01	mIoUL @0.01	mIoUL @0.05	IAUC mIoU	DAUC mIoU	Diff.	IAUC Conf @0.01	mIoUL @0.01
DCAMA	Random	47.50	46.85	0.65	43.36	41.42	31.62	71.35	70.77	0.59	41.71	55.24	33.42
	Gaussian Noise Mask	52.32	15.46	36.86	53.80	31.08	17.71	74.67	23.36	51.31	55.32	35.65	15.86
	Saliency [35]	52.02	41.10	10.92	44.97	37.01	23.73	72.99	66.73	6.27	44.32	46.42	24.46
	Integrated Gradients [40]	49.23	45.97	3.27	45.63	34.18	22.25	72.38	70.22	2.16	42.94	45.01	23.26
	Guided IG [16]	50.77	45.10	5.67	51.25	30.17	21.65	71.74	70.35	1.39	49.08	42.53	23.19
	Blur IG [48]	52.40	41.63	10.78	44.25	36.69	22.84	73.82	65.80	8.01	42.23	46.86	21.53
	XRAI [15]	54.45	38.72	15.73	51.98	26.59	12.08	75.52	60.98	14.55	56.12	26.25	8.55
	Deep Lift [34]	49.78	48.51	1.27	44.80	36.67	24.07	72.72	71.66	1.06	44.19	45.82	22.83
	LIME [30]	53.18	48.44	4.73	47.98	32.44	15.29	74.77	72.20	2.57	49.19	36.71	13.40
	Unmasked AffEx (ours)	54.85	28.26	26.59	60.82	17.41	8.85	76.23	46.34	29.89	66.82	13.78	5.72
Masked AffEx (ours)	52.32	15.06	37.26	62.60	16.43	12.27	73.16	21.19	51.97	67.91	13.71	7.09	
Signed AffEx (ours)	53.24	23.77	29.48	60.49	19.40	13.67	75.46	45.45	30.01	66.60	13.93	7.82	
DMTNet	Random	21.21	20.98	0.23	60.36	24.93	31.88	29.01	28.46	0.55	60.35	33.89	46.01
	Gaussian Noise Mask	39.08	15.71	23.37	59.35	20.69	13.26	54.53	24.41	30.12	59.90	33.24	31.00
	Saliency [35]	36.51	26.79	9.72	63.09	21.05	15.77	52.43	41.22	11.21	64.85	29.85	25.49
	Integrated Gradients [40]	26.25	19.47	6.78	62.51	21.63	20.32	37.13	29.08	8.05	63.99	30.31	33.07
	Blur IG [48]	35.04	20.32	14.72	62.17	21.54	20.20	47.83	33.82	14.01	63.62	29.77	33.13
	XRAI [15]	38.19	26.55	11.64	68.42	16.48	10.73	55.82	45.72	10.09	69.78	20.03	12.88
	LIME [30]	36.83	32.44	4.39	70.72	19.20	11.36	54.76	49.80	4.96	70.56	23.46	12.43
	Unmasked AffEx (ours)	40.10	17.09	23.01	67.30	10.53	4.49	58.16	28.81	29.35	66.80	13.34	5.32
	Masked AffEx (ours)	40.52	16.38	24.14	67.23	9.95	3.10	58.47	26.87	31.60	66.94	12.78	4.62
	Signed AffEx (ours)	38.85	18.81	20.03	67.16	10.49	3.72	57.58	35.68	21.90	68.05	13.16	6.38

Table 1. Results of the interpretability evaluation on the COCO 20ⁱ and Pascal 5ⁱ datasets under 1-way 5-shot. The table shows the Insertion Area Under the Curve (IAUC), Deletion Area Under the Curve (DAUC), their difference (Diff. \uparrow), the IAUC@0.01 \uparrow , the mIoULoss@0.01 \downarrow , and the mIoULoss@0.05 \downarrow . The best results are highlighted in bold, except for IAUC and DAUC, as their values are not directly comparable alone.

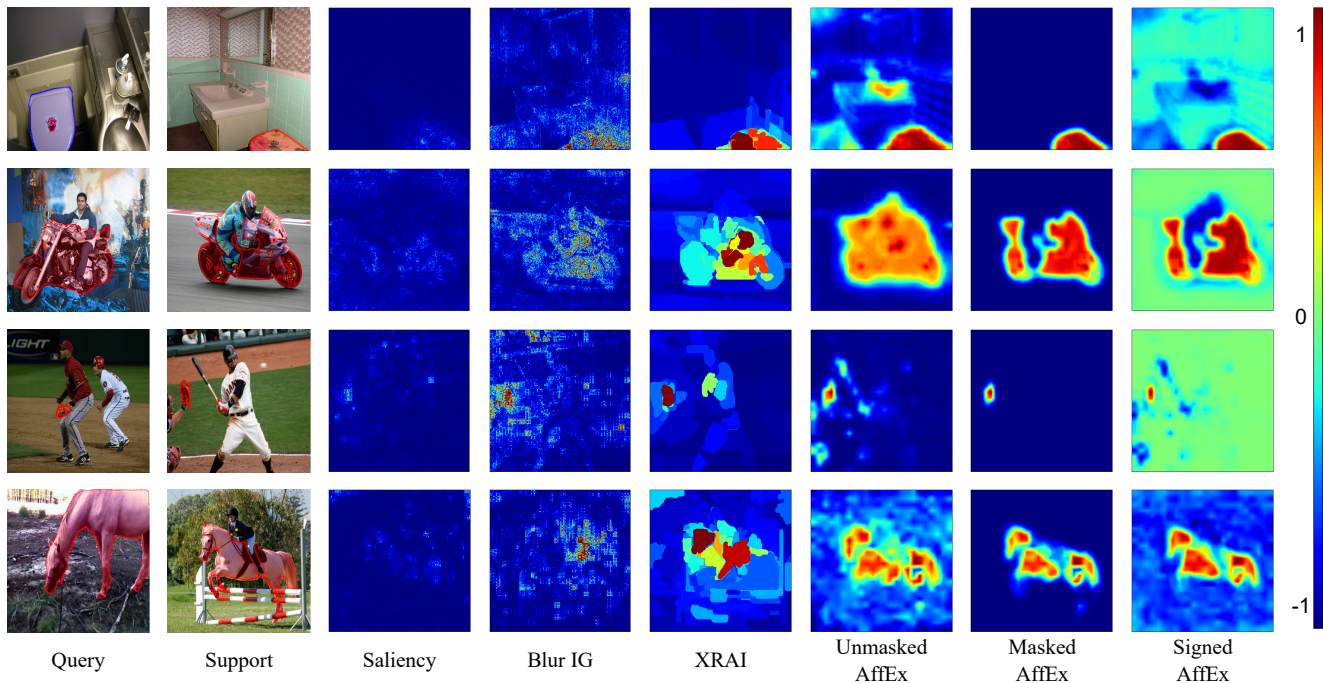


Figure 2. A 1-way 1-shot example of Saliency, Blur IG, XRAI, Unmasked Affex, Masked Affex, and Signed Affex for the two tested models DMTNet (first two rows) and DCAMA (last two rows) over four different episodes. The prediction is highlighted in red over the query image, and the ground truth is shown in blue only when it differs significantly from the prediction.

qualitative results, with 5-shots examples, are provided in the supplementary material.

Dataset	COCO 20 ⁱ		Pascal 5 ⁱ	
	mIoUL @0.01	mIoUL @0.05	mIoUL @0.01	mIoUL @0.05
Explanation Method				
	DCAMA			
Random	33.79	29.78	48.72	34.64
Gaussian Noise Mask	27.07	12.96	33.6	16.01
Saliency [35]	33.93	24.13	50.06	32.8
Integrated Gradients [40]	32.19	22.61	44.41	27.53
Guided IG [16]	25.96	19.49	41.33	29.58
Blur IG [48]	33.89	23.29	47.96	28.61
XRAI [15]	29.65	14.5	37.49	13.25
Deep Lift [34]	32.6	24.85	46.76	28.93
LIME [30]	27.27	13.44	40.03	13.97
Unmasked AffEx (ours)	19.84	10.08	22.85	7.9
Masked AffEx (ours)	17.63	8.11	19.33	7.32
Signed AffEx (ours)	18.71	9.82	21.8	9.72
	DMTNet			
Random	23.53	26.01	35.79	41.19
Gaussian Noise Mask	16.2	8.66	31.02	23.73
Saliency [35]	20.15	17.46	33.3	35.59
Integrated Gradients [40]	20.53	20.81	32.03	37.64
Blur IG[48]	20.22	17.42	31.56	35.04
XRAI [15]	14.83	6.3	20.56	10.8
Deep Lift [34]	20.81	22.25	32.1	39.42
LIME [30]	14.84	8.32	22.95	10.4
Unmasked AffEx (ours)	10.97	4.14	16.35	7.85
Masked AffEx (ours)	10.09	3.77	16.49	7.88
Signed AffEx (ours)	11.12	3.8	16.36	7.85

Table 2. mIoULoss@ p results for the interpretability evaluation on the COCO 20ⁱ and Pascal 5ⁱ in the 1-way 1-shot setting. The table shows the mIoULoss@0.01 \downarrow and mIoULoss@0.05 \downarrow . The best results are highlighted in bold.

4.3. Ablation Study

The softmax was employed to transform the raw matching scores into a probability distribution over the support images. This normalization enables an interpretable view of the matching scores as relative contributions of each support sample to the query prediction. To evaluate its impact, we removed the softmax layer and used the unnormalized scores directly. Experiments were conducted on the PASCAL-5ⁱ dataset using the DCAMA model in a 1-way 5-shot setting. We report mIoULoss@ p for $p \in 0.01, 0.05$, observing a degradation of 12.58 and 5.09 points, respectively. In contrast, no degradation is observed with DMTNet under the same settings, as its correlation-based matching is inherently normalized.

The results differ for the Feature Ablation component. We ablated it by replacing the learned importance weighting with a simpler mean aggregation. This modification did not result in significant performance drop. Although each model exhibits different biases toward specific feature levels, averaging provides a sufficient numerical approximation of per-feature contributions. Nevertheless, we retained the Feature Ablation mechanism, as it produces qualitatively superior heatmaps by suppressing irrelevant regions such as background clutter and non-discriminative areas, which is critical for reliable interpretability.

IAUC and DAUC are metrics that approximate an area

Metric	N. Steps Method	5	10	25	50	75	100
		DAUC	Saliency	6.44	3.85	1.91	1.16
	AffEx	9.04	5.37	3.12	1.85	1.37	1.10
IAUC	Saliency	6.33	3.63	2.14	1.32	0.98	0.75
	AffEx	6.64	3.22	1.34	0.77	0.59	0.46

Table 3. Relative error on the 95% percentile of the Insertion Area Under the Curve (IAUC) and Deletion Area Under the Curve (DAUC) metrics with respect to the ground truth value obtained with 1000 steps. The table shows the relative error for the Affinity Explainer (AffEx) and Saliency methods. The lower the relative error, the more stable the metric is with respect to the number of steps.

under the curve. Thus, they require several steps to compute the area. Each of these steps requires evaluating the model, which can be expensive depending on the model used. Furthermore, the model’s confidence may fluctuate when adding or removing pixels, making it difficult to determine the correct approximation. To address this issue, we performed an ablation study on the number of steps used to compute the IAUC and DAUC metrics. We varied the number of steps from 5 to 1000, using the value obtained with 1000 steps as the ground truth, and computed the relative error with respect to the ground truth. We evaluated this ablation on the Pascal 5ⁱ dataset, using the DCAMA model and the Affinity Explainer and Saliency methods. We calculated the 95% percentile to find an upper bound of the relative error. Table 3 shows the results of the ablation study on the number of steps used to compute the IAUC and DAUC metrics. As the number of steps increases, the relative error decreases, indicating that the metrics become more stable with an increasing number of steps. As a trade-off between computational cost and stability, we suggest using 75 steps for all the other experiments.

5. Conclusion

In this work, we introduced a novel method for interpreting Few-Shot Semantic Segmentation models, grounded in the matching operations that underlie their design. Our approach exploits the intrinsic structure of matching-based FSS models to generate interpretable segmentation maps that highlight the contribution of each support image to the final prediction. We further proposed a causal evaluation framework for assessing interpretability in FSS, employing quantitative metrics such as the IAUC and DAUC, their difference, and the mIoULoss family of measures. Through an extensive benchmark across multiple datasets and attribution baselines, we demonstrated that our method consistently outperforms existing explainability techniques, both quantitatively and qualitatively. The qualitative results demonstrate that our approach reveals how support exam-

ples influence query segmentation, providing actionable insight into model behavior. Additionally, our ablation study on the number of integration steps confirms the robustness and stability of our evaluation framework.

Overall, this work advances the understanding of interpretability in few-shot segmentation by offering both a principled evaluation protocol and an effective attribution method. Future directions include extending our framework to a broader range of FSS architectures and integrating it with complementary explainability strategies to enhance interpretability and diagnostic power further.

References

- [1] Michelangelo Acconci and Stavros Ntalampiras. One-shot learning for acoustic identification of bird species in non-stationary environments. In *2020 25th International Conference on Pattern Recognition (ICPR)*, pages 755–762. IEEE, 2021. 3
- [2] Radhakrishna Achanta, Appu Shaji, Kevin Smith, Aurelien Lucchi, Pascal Fua, and Sabine Süsstrunk. SLIC Superpixels Compared to State-of-the-Art Superpixel Methods. *IEEE Transactions on Pattern Analysis and Machine Intelligence*, 34(11):2274–2282, 2012. 1
- [3] Sebastian Bach, Alexander Binder, Grégoire Montavon, Frederick Klauschen, Klaus-Robert Müller, and Wojciech Samek. On pixel-wise explanations for non-linear classifier decisions by layer-wise relevance propagation. *PLoS one*, 10(7):e0130140, 2015. 3
- [4] Jiayi Chen, Rong Quan, and Jie Qin. Cross-Domain Few-Shot Semantic Segmentation via Doubly Matching Transformation. In *Proceedings of the Thirty-Third International Joint Conference on Artificial Intelligence*, pages 641–649, Jeju, South Korea, 2024. International Joint Conferences on Artificial Intelligence Organization. 3, 5, 1, 2
- [5] Xu Cheng, Haoyuan Li, Shuya Deng, and Yonghong Peng. POEM: A prototype cross and emphasis network for few-shot semantic segmentation. *Computer Vision and Image Understanding*, 234:103746, 2023. 2, 6
- [6] Pasquale De Marinis, Nicola Fanelli, Raffaele Scaringi, Emanuele Colonna, Giuseppe Fiameni, Gennaro Vessio, and Giovanna Castellano. Label Anything: Multi-Class Few-Shot Semantic Segmentation with Visual Prompts. In *ECAI 2025*, pages 4016–4023. IOS Press, 2025. 2
- [7] Henghui Ding, Hui Zhang, and Xudong Jiang. Self-regularized prototypical network for few-shot semantic segmentation. *Pattern Recognition*, 133:109018, 2023. 2, 6
- [8] Dumitru Erhan, Yoshua Bengio, Aaron Courville, and Pascal Vincent. Visualizing higher-layer features of a deep network. *University of Montreal*, 1341(3):1, 2009. 3
- [9] Andrea Fedele. Explain and Interpret Few-Shot Learning. In *xAI (Late-breaking Work, Demos, Doctoral Consortium)*, pages 233–240, 2023. 3
- [10] Chelsea Finn, Pieter Abbeel, and Sergey Levine. Model-Agnostic Meta-Learning for Fast Adaptation of Deep Networks, 2017. arXiv:1703.03400 [cs]. 2
- [11] Ruth Fong, Mandela Patrick, and Andrea Vedaldi. Understanding deep networks via extremal perturbations and smooth masks. In *Proceedings of the IEEE/CVF international conference on computer vision*, pages 2950–2958, 2019. 3
- [12] Shir Gur, Ameen Ali, and Lior Wolf. Visualization of supervised and self-supervised neural networks via attribution guided factorization. In *Proceedings of the AAAI conference on artificial intelligence*, pages 11545–11554, 2021. 3
- [13] Brian Kenji Iwana, Ryohei Kuroki, and Seiichi Uchida. Explaining convolutional neural networks using softmax gradient layer-wise relevance propagation. In *2019 IEEE/CVF International Conference on Computer Vision Workshop (ICCVW)*, pages 4176–4185. IEEE, 2019. 3
- [14] Uday Kamath, John Liu, and James Whitaker. *Deep Learning for NLP and Speech Recognition*. Springer International Publishing, Cham, 2019. 1
- [15] Andrei Kapishnikov, Tolga Bolukbasi, Fernanda Viegas, and Michael Terry. XRAI: Better Attributions Through Regions. In *2019 IEEE/CVF International Conference on Computer Vision (ICCV)*, pages 4947–4956, Seoul, Korea (South), 2019. IEEE. 5, 7, 8, 1
- [16] Andrei Kapishnikov, Subhashini Venugopalan, Besim Avci, Ben Wedin, Michael Terry, and Tolga Bolukbasi. Guided Integrated Gradients: An Adaptive Path Method for Removing Noise. pages 5050–5058, 2021. 5, 7, 8, 1
- [17] Chunbo Lang, Gong Cheng, Binfei Tu, and Junwei Han. Learning What Not to Segment: A New Perspective on Few-Shot Segmentation. In *2022 IEEE/CVF Conference on Computer Vision and Pattern Recognition (CVPR)*, pages 8047–8057, New Orleans, LA, USA, 2022. IEEE. 1, 2
- [18] Gen Li, Varun Jampani, Laura Sevilla-Lara, Deqing Sun, Jonghyun Kim, and Joongkyu Kim. Adaptive Prototype Learning and Allocation for Few-Shot Segmentation. In *2021 IEEE/CVF Conference on Computer Vision and Pattern Recognition (CVPR)*, pages 8330–8339, Nashville, TN, USA, 2021. IEEE. 2
- [19] Liangzhi Li, Bowen Wang, Manisha Verma, Yuta Nakashima, Ryo Kawasaki, and Hajime Nagahara. Scouter: Slot attention-based classifier for explainable image recognition. In *Proceedings of the IEEE/CVF international conference on computer vision*, pages 1046–1055, 2021. 3
- [20] Chen Liang and Shuang Bai. Found missing semantics: Supplemental prototype network for few-shot semantic segmentation. *Computer Vision and Image Understanding*, 249:104191, 2024. 2
- [21] Scott M Lundberg and Su-In Lee. A unified approach to interpreting model predictions. *CoRR*, abs/1705.07874, 2017. 3
- [22] Juhong Min, Dahyun Kang, and Minsu Cho. Hypercorrelation Squeeze for Few-Shot Segmentation. 1, 2
- [23] Volodymyr Mnih, Koray Kavukcuoglu, David Silver, Andrei A Rusu, Joel Veness, Marc G Bellemare, Alex Graves, Martin Riedmiller, Andreas K Fidjeland, Georg Ostrovski, et al. Human-level control through deep reinforcement learning. *nature*, 518(7540):529–533, 2015. 1

- [24] Grégoire Montavon, Sebastian Lapuschkin, Alexander Binder, Wojciech Samek, and Klaus-Robert Müller. Explaining nonlinear classification decisions with deep taylor decomposition. *Pattern recognition*, 65:211–222, 2017. 3
- [25] Woo-Jeoung Nam, Shir Gur, Jaesik Choi, Lior Wolf, and Seong-Whan Lee. Relative attributing propagation: Interpreting the comparative contributions of individual units in deep neural networks. In *Proceedings of the AAAI conference on artificial intelligence*, pages 2501–2508, 2020. 3
- [26] Khoi Nguyen and Sinisa Todorovic. Feature weighting and boosting for few-shot segmentation. In *Proceedings of the IEEE/CVF International Conference on Computer Vision*, pages 622–631, 2019. 6, 3
- [27] Frank Pasquale. *The black box society: The secret algorithms that control money and information*. Harvard University Press, 2015. 1
- [28] Bohao Peng, Zhuotao Tian, Xiaoyang Wu, Chengyao Wang, Shu Liu, Jingyong Su, and Jiaya Jia. Hierarchical Dense Correlation Distillation for Few-Shot Segmentation. In *2023 IEEE/CVF Conference on Computer Vision and Pattern Recognition (CVPR)*, pages 23641–23651, Vancouver, BC, Canada, 2023. IEEE. 3
- [29] Vitali Petsiuk. RISE: Randomized Input Sampling for Explanation of Black-box Models. 5
- [30] Marco Tulio Ribeiro, Sameer Singh, and Carlos Guestrin. “Why Should I Trust You?”: Explaining the Predictions of Any Classifier. In *Proceedings of the 22nd ACM SIGKDD International Conference on Knowledge Discovery and Data Mining*, pages 1135–1144, New York, NY, USA, 2016. Association for Computing Machinery. 3, 5, 7, 8, 1
- [31] Ramprasaath R. Selvaraju, Michael Cogswell, Abhishek Das, Ramakrishna Vedantam, Devi Parikh, and Dhruv Batra. Grad-CAM: Visual Explanations From Deep Networks via Gradient-Based Localization. pages 618–626, 2017. 3, 5, 6
- [32] Amirreza Shaban, Shray Bansal, Zhen Liu, Irfan Essa, and Byron Boots. One-Shot Learning for Semantic Segmentation, 2017. arXiv:1709.03410 [cs]. 6, 3
- [33] Xinyu Shi, Dong Wei, Yu Zhang, Donghuan Lu, Munan Ning, Jiashun Chen, Kai Ma, and Yefeng Zheng. Dense Cross-Query-and-Support Attention Weighted Mask Aggregation for Few-Shot Segmentation. In *Computer Vision – ECCV 2022*, pages 151–168. Springer Nature Switzerland, Cham, 2022. Series Title: Lecture Notes in Computer Science. 1, 2, 3, 5
- [34] Avanti Shrikumar, Peyton Greenside, and Anshul Kundaje. Learning Important Features Through Propagating Activation Differences. In *Proceedings of the 34th International Conference on Machine Learning*, pages 3145–3153. PMLR, 2017. ISSN: 2640-3498. 5, 7, 8, 1
- [35] Karen Simonyan. Deep inside convolutional networks: Visualising image classification models and saliency maps. *arXiv preprint arXiv:1312.6034*, 2013. 5, 7, 8, 1
- [36] Daniel Smilkov, Nikhil Thorat, Been Kim, Fernanda Viégas, and Martin Wattenberg. Smoothgrad: removing noise by adding noise. *arXiv preprint arXiv:1706.03825*, 2017. 3
- [37] Jake Snell, Kevin Swersky, and Richard S. Zemel. Prototypical Networks for Few-shot Learning, 2017. arXiv:1703.05175 [cs, stat]. 2
- [38] Suraj Srinivas and François Fleuret. Full-gradient representation for neural network visualization. *Advances in neural information processing systems*, 32, 2019. 3
- [39] Jiamei Sun, Sebastian Lapuschkin, Wojciech Samek, Yunqing Zhao, Ngai-Man Cheung, and Alexander Binder. Explanation-guided training for cross-domain few-shot classification. In *2020 25th international conference on pattern recognition (ICPR)*, pages 7609–7616. IEEE, 2021. 3
- [40] Mukund Sundararajan, Ankur Taly, and Qiqi Yan. Axiomatic attribution for deep networks. In *International conference on machine learning*, pages 3319–3328. PMLR, 2017. 5, 7, 8, 1
- [41] Flood Sung, Yongxin Yang, Li Zhang, Tao Xiang, Philip H. S. Torr, and Timothy M. Hospedales. Learning to Compare: Relation Network for Few-Shot Learning, 2018. arXiv:1711.06025 [cs]. 2
- [42] Lev Utkin, Maxim Kovalev, and Ernest Kasimov. Explanation of siamese neural networks for weakly supervised learning. *Computing and Informatics*, 39(6):1172–1202, 2020. 3
- [43] Oriol Vinyals, Charles Blundell, Timothy Lillicrap, Koray Kavukcuoglu, and Daan Wierstra. Matching Networks for One Shot Learning, 2017. arXiv:1606.04080 [cs, stat]. 2
- [44] Bowen Wang, Liangzhi Li, Manisha Verma, Yuta Nakashima, Ryo Kawasaki, and Hajime Nagahara. MTUNet: Few-shot image classification with visual explanations. In *Proceedings of the IEEE/CVF Conference on Computer Vision and Pattern Recognition*, pages 2294–2298, 2021. 3
- [45] Bowen Wang, Liangzhi Li, Manisha Verma, Yuta Nakashima, Ryo Kawasaki, and Hajime Nagahara. Match them up: visually explainable few-shot image classification. *Applied Intelligence*, 53(9):10956–10977, 2023. 3
- [46] Kaixin Wang, Jun Hao Liew, Yingtian Zou, Daquan Zhou, and Jiashi Feng. PANet: Few-Shot Image Semantic Segmentation With Prototype Alignment. In *2019 IEEE/CVF International Conference on Computer Vision (ICCV)*, pages 9196–9205, Seoul, Korea (South), 2019. IEEE. 2, 6
- [47] Yaqing Wang, Quanming Yao, James T Kwok, and Lionel M Ni. Generalizing from a few examples: A survey on few-shot learning. *ACM computing surveys (csur)*, 53(3):1–34, 2020. 1, 2
- [48] Shawn Xu, Subhashini Venugopalan, and Mukund Sundararajan. Attribution in Scale and Space. pages 9680–9689, 2020. 5, 7, 8, 1
- [49] Boyu Yang, Chang Liu, Bohao Li, Jianbin Jiao, and Qixiang Ye. Prototype Mixture Models for Few-Shot Semantic Segmentation. In *Computer Vision – ECCV 2020*, pages 763–778, Cham, 2020. Springer International Publishing. 2
- [50] Lihe Yang, Wei Zhuo, Lei Qi, Yinghuan Shi, and Yang Gao. Mining Latent Classes for Few-Shot Segmentation. pages 8721–8730, 2021. 2, 6
- [51] Tom Young, Devamanyu Hazarika, Soujanya Poria, and Erik Cambria. Recent trends in deep learning based natural language processing. *IEEE Computational Intelligence Magazine*, 13(3):55–75, 2018. 1

- [52] Gengwei Zhang, Guoliang Kang, Yi Yang, and Yunchao Wei. Few-Shot Segmentation via Cycle-Consistent Transformer. In *Advances in Neural Information Processing Systems*, pages 21984–21996. Curran Associates, Inc., 2021. [1](#), [2](#)
- [53] Jianming Zhang, Sarah Adel Bargal, Zhe Lin, Jonathan Brandt, Xiaohui Shen, and Stan Sclaroff. Top-down neural attention by excitation backprop. *International Journal of Computer Vision*, 126(10):1084–1102, 2018. [3](#)
- [54] Xiaolin Zhang, Yunchao Wei, Yi Yang, and Thomas S. Huang. SG-One: Similarity Guidance Network for One-Shot Semantic Segmentation. *IEEE Transactions on Cybernetics*, 50(9):3855–3865, 2020. Conference Name: IEEE Transactions on Cybernetics. [2](#), [6](#)
- [55] Xin-Yi Zhang, Xian-Kai Lu, Yi-Long Yin, Han-Jia Ye, and De-Chuan Zhan. Efficient Sampling-based Gaussian Processes for few-shot semantic segmentation. *Pattern Recognition*, 164:111542, 2025. [1](#), [2](#)
- [56] Bolei Zhou, David Bau, Aude Oliva, and Antonio Torralba. Interpreting deep visual representations via network dissection. *IEEE transactions on pattern analysis and machine intelligence*, 41(9):2131–2145, 2018. [3](#)

Matching-Based Few-Shot Semantic Segmentation Models Are Interpretable by Design

Supplementary Material

S.1. Considerations on Computational Cost

The computational efficiency of interpretability methods is often overlooked. However, it is a decisive factor for their applicability in real-world systems, especially when dealing with high-resolution data or real-time requirements. This section analyzes the computational costs of our proposed Affinity Explainer (AffEx) in comparison with widely used interpretability techniques: Saliency Maps [35], Integrated Gradients [40], Guided Integrated Gradients [16], XRAI [15], Blur IG [48], Deep Lift [34], and LIME [30]. We omit separate results for the three AffEx variants, as their computational differences are negligible.

We evaluated both the memory consumption and inference time required to produce explanations for two state-of-the-art few-shot segmentation models, DCAMA [33] and DMTNet [4], under 1-shot and 5-shot settings. All experiments were conducted on an NVIDIA A100 GPU.

As reported in Tab. S.1, AffEx achieves a favorable trade-off between memory efficiency and computational latency. While not as lightweight as Saliency Maps, AffEx significantly outperforms gradient-based methods like Integrated Gradients and its variants in terms of speed, reducing inference time by an order of magnitude. This efficiency stems from AffEx’s design, which leverages pre-computed similarity maps and avoids multiple backward passes through the network. In terms of memory usage, AffEx maintains a moderate footprint, requiring less memory than Deep Lift, which is the most memory-intensive method evaluated.

Overall, AffEx provides a balanced efficiency profile, remaining close to real-time operation while preserving interpretability quality. This efficiency makes AffEx suitable for deployment in scenarios constrained by limited GPU resources or strict latency requirements, where traditional backpropagation-based explainers are computationally demanding. Furthermore, we conducted an ablation study on the resolution of the similarity maps used in AffEx, demonstrating that computational cost can be further optimized without significantly compromising interpretability, as detailed in Sec. S.3.

S.2. Adapting LIME to Few-Shot Segmentation

While gradient-based and perturbation-based attribution methods can be directly applied to Few-Shot Segmentation (FSS) models with minor modifications, adapting model-

agnostic approaches such as LIME [30] requires a more careful formulation. We adapted the LIME framework to the FSS setting, where predictions depend jointly on a query image and a structured support set. The interpretable feature space is defined as a binary activation vector over the M support examples, where each entry indicates whether a given support image and its mask are included in the conditioning set, while the query remains fixed. Perturbations are generated by randomly masking subsets of supports following a Bernoulli process, with removed elements replaced by zero-valued baselines. The model is then evaluated on each perturbed configuration to fit a local linear surrogate model around the original prediction.

To preserve spatial interpretability on the query, the image was partitioned into superpixels using the SLIC algorithm [2], which provides the feature mask for LIME. Each superpixel corresponds to an interpretable unit that can be independently switched on or off during perturbation, ensuring that the explanation remains coherent with perceptual boundaries.

Locality between the original support set $S = \{(x_i, m_i)\}_{i=1}^M$ and a perturbed configuration S' was enforced through a composite distance:

$$D(S, S') = \frac{1}{M} \sum_{i=1}^M [\lambda(1 - \cos(x_i, x'_i)) + (1 - \lambda) \Delta_{fg}(m_i, m'_i)], \quad (\text{S.1})$$

where $\cos(\cdot, \cdot)$ measures cosine similarity between support images and perturbed support images, Δ_{fg} quantifies the fraction of foreground pixels removed in each perturbed mask. The hyperparameter $\lambda \in [0, 1]$ serves as a balancing weight to adjust the relative influence of the visual dissimilarity (image-based) and the mask dissimilarity (mask-based) components of the overall distance. Missing supports are assigned maximal dissimilarity ($D_i = 1$). The corresponding kernel weight is

$$w(S, S') = \exp\left(-\frac{D(S, S')^2}{\sigma^2}\right), \quad (\text{S.2})$$

with σ controlling the width of the locality kernel. This adaptation allows LIME to account for the dual conditioning structure of FSS, producing explanations that remain localized in both spatial and semantic terms. To find the optimal parameters K (number of superpixels), λ , and σ , we performed a grid search on Pascal 5ⁱ in a 5-shot setting, optimizing for mIoULoss@0.01. Results are reported in Tab. S.2. We report results only for the best λ as it had

Model	Explanation Method	1 shot		5 shots	
		Expl. Mem. (GB)	Expl. Time (ms)	Expl. Mem. (GB)	Expl. Time (ms)
DCAMA	Forward Pass	1.85 ± 0.00	44 ± 1	6.37 ± 0.00	109 ± 1
	Saliency	4.00 ± 0.00	102 ± 1	13.70 ± 0.00	284 ± 2
	Integrated Gradients	4.01 ± 0.00	2571 ± 40	13.76 ± 0.00	7154 ± 103
	Guided IG	4.00 ± 0.00	3693 ± 34	13.70 ± 0.00	11079 ± 78
	Blur IG	4.00 ± 0.00	11904 ± 56	13.70 ± 0.00	35268 ± 163
	XRAI	4.00 ± 0.00	13076 ± 1469	13.70 ± 0.00	37647 ± 3645
	Deep Lift	6.93 ± 0.00	146 ± 1	24.09 ± 0.01	442 ± 2
	LIME	1.85 ± 0.00	1432 ± 91	6.30 ± 0.00	3627 ± 98
	AffEx (ours)	3.33 ± 0.21	182 ± 5	13.90 ± 1.03	552 ± 28
DMTNet	Forward Pass	0.83 ± 0.00	142 ± 1	2.67 ± 0.00	667 ± 19
	Saliency	6.49 ± 0.00	206 ± 2	20.17 ± 0.00	1039 ± 90
	Integrated Gradients	6.51 ± 0.00	5141 ± 135	20.23 ± 0.00	27096 ± 375
	Blur IG	6.45 ± 0.00	15153 ± 114	19.97 ± 0.00	55707 ± 410
	XRAI	6.45 ± 0.00	16735 ± 1569	19.97 ± 0.00	58245 ± 4145
	Deep Lift	12.92 ± 0.00	279 ± 2	-	-
	LIME	0.85 ± 0.00	5087 ± 93	2.76 ± 0.00	22717 ± 1039
	AffEx (ours)	2.38 ± 0.22	427 ± 5	11.13 ± 0.84	2072 ± 20

Table S.1. Computational cost comparison between AffEx and other interpretability methods, including Integrated Gradients, Saliency Maps, and Deep Lift. The table reports the average memory consumption (in GB) and time (in milliseconds) for generating explanations, along with the forward pass time of the models for reference. The forward pass cost is shown in a gray background. The results are presented for both 1-shot and 5-shot scenarios, with standard deviations included. The experiments were conducted on an NVIDIA A100.

a marginal effect on performance. The best configuration uses 160 superpixels, Ridge regression, $\sigma=0.5$, and $\lambda=0.2$.

S.3. Coarse vs. Fine Attribution Maps

We investigated how the resolution of attribution maps affects both interpretability and computational cost. Affinity Explainer extracts attribution maps from intermediate similarity maps, which must be interpolated to a common resolution before aggregation. The choice of this resolution influences the quality of explanations and the computational resources required, as these maps are 5D tensors of size $H \times W \times H_s \times W_s \times M$.

To systematically study this trade-off, we evaluated similarity map resolutions ranging from coarse (32×32) to fine (256×256), as well as the native resolution of each backbone (400×400 for DMTNet [4] and 384×384 for DCAMA [33]). Results are summarized in Fig. S.1.

We observe model-dependent behaviors. For DCAMA, higher resolution improves interpretability at the cost of increased computation, consistent with expectations. Conversely, DMTNet exhibits the opposite trend: coarser resolutions yield smoother, less noisy attribution maps by filtering out fine-grained details that are less relevant to the model’s overall attention patterns. As illustrated in the main paper’s examples, DMTNet primarily attends to entire objects rather than fine details, making its coarser maps more

representative of its internal reasoning. DCAMA, which emphasizes finer details, benefits from higher resolution, though differences in $mIoULoss@0.01$ remain marginal, indicating that Affinity Explainer is robust to this hyperparameter.

From a computational perspective, reducing resolution substantially decreases inference time: for DCAMA, latency drops from 552ms at 256×256 to 180ms at 32×32 , while DMTNet ranges from 2072ms to 1724ms over the same resolutions. Memory consumption scales approximately linearly with resolution, plateauing at 64×64 due to fixed-size intermediate tensors. Specifically, memory usage increases from 3.25GB to 11.13GB for DMTNet and from 6.68GB to 13.90GB for DCAMA when moving from 32×32 to 256×256 .

Overall, these findings highlight the need to select a similarity map resolution that aligns with both the model’s characteristics and computational constraints, enabling an informed balance between interpretability and resource efficiency.

S.4. Additional Qualitative Samples

This section presents additional qualitative examples complementing the interpretability analysis discussed in the main paper. All visualizations were generated using the Signed AffEx method. Figure S.2 shows examples pro-

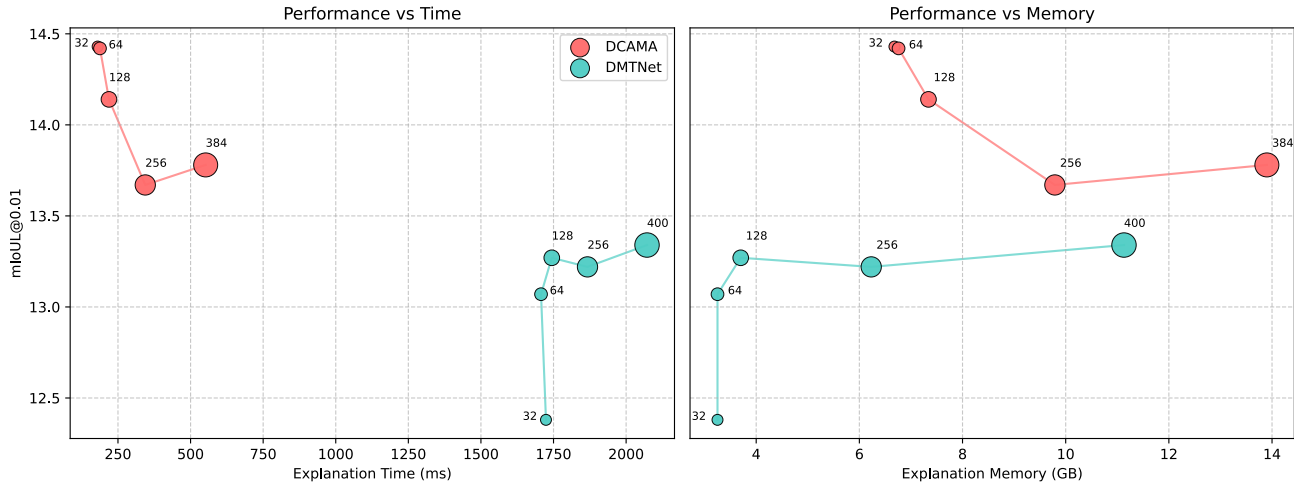


Figure S.1. Ablation study on the impact of similarity map resolution on interpretability quality (mIoULoss@0.01) and computational cost (inference time in ms) for AffEx applied to DMTNet [4] and DCAMA [33]. The results highlight the trade-off between attribution mIoUL@0.01 and resource consumption across different resolutions.

Superpixels	Model	Kernel width (σ)	Image-Mask balance (λ)	mIoUL@0.01
80	Lasso	0.5	0.2	37.54
		0.5	0.5	37.65
		0.5	0.8	37.39
	Lasso	1.0	0.2	37.24
		1.0	0.5	37.19
		1.0	0.8	37.23
	Ridge	0.5	0.2	36.31
		0.5	0.8	36.83
		3.0	0.5	36.46
160	Lasso	0.5	0.2	37.47
		0.5	0.5	37.16
		0.5	0.8	36.63
	Lasso	1.0	0.2	36.36
		1.0	0.5	36.54
		1.0	0.8	36.52
	Ridge	0.5	0.2	33.82
		0.5	0.8	33.97
		3.0	0.5	34.05

Table S.2. Grid search results for adapting LIME to few-shot segmentation. The table reports the mIoULoss@0.01 for different configurations of superpixels, regression models (Lasso or Ridge), kernel width (σ), and the balance parameter (λ). The best performance is highlighted in bold.

duced with DCAMA, while Fig. S.3 reports the corresponding results for DMTNet, both evaluated on the COCO-20ⁱ [26] and PASCAL-5ⁱ [32] datasets. Each figure includes a

series of query–support pairs illustrating the models’ predicted segmentations together with their corresponding attribution maps. The first and third episodes are shared between the two figures to facilitate a direct comparison of how attributions differ across models.

S.5. IAUC and DAUC Plots

To better illustrate how IAUC and DAUC reflect attribution quality, we provide additional visualizations of their corresponding curves. Figure S.4 and Figure S.5 show two examples of Insertion and Deletion curves for DCAMA on COCO-20ⁱ. Each example includes the IAUC and DAUC plots, the model’s confidence map, the segmented query image (prediction in red, ground truth in blue), and the support set with corresponding masks (in red). For the first episode in Fig. S.4, we display only the initial IAUC step, as the remainder of the curve is nearly flat. In this case, the pixels selected by Signed AffEx quickly lead to a high-quality segmentation, producing a steep IAUC curve. The DAUC curve, by contrast, decreases more gradually and exhibits small oscillations as pixels are removed, indicating that the model can still rely on the remaining support information to maintain a reasonable prediction. This is further confirmed by the DAUC-step confidence maps: even after removing the most influential pixels, the model retains partial segmentation ability, suggesting either an inherent foreground bias or a dependence on broader contextual cues (e.g., the sea) that guide the prediction toward the boat. Such episodes are common in the 5-shot setting, which motivates the use of IAUC@p and mIoULoss@p to better capture early differences in the curves.

The second episode in Fig. S.5 shows a slower IAUC

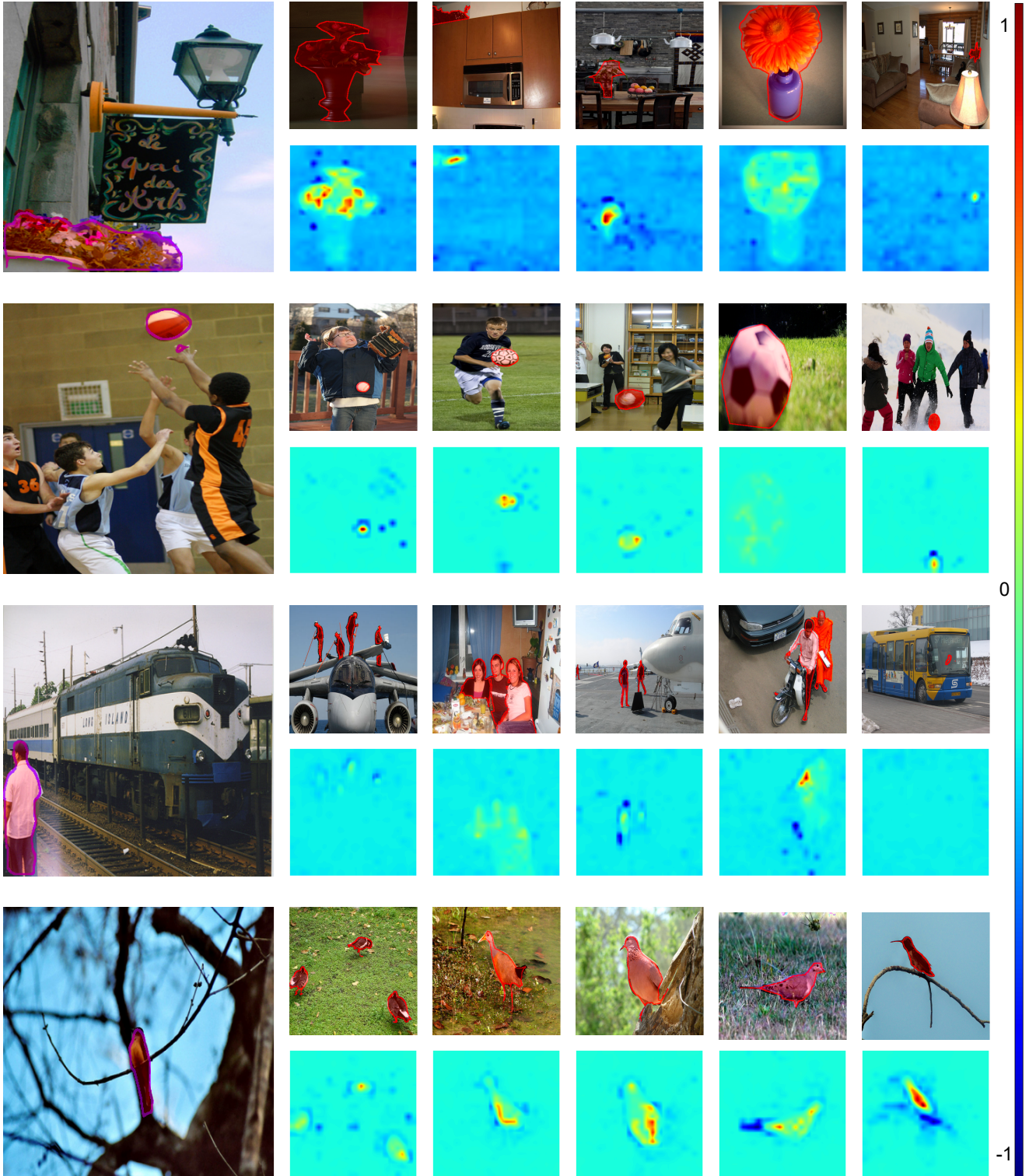


Figure S.2. Qualitative results for Signed AffEx with DCAMA across multiple episodes from COCO-20ⁱ (first two rows) and Pascal-5ⁱ (last two rows). For each episode, the left column shows the query image with the predicted segmentation in red; the ground truth is overlaid in blue when it significantly differs from the prediction. The right column presents the corresponding support set alongside the attribution maps produced by the proposed method.

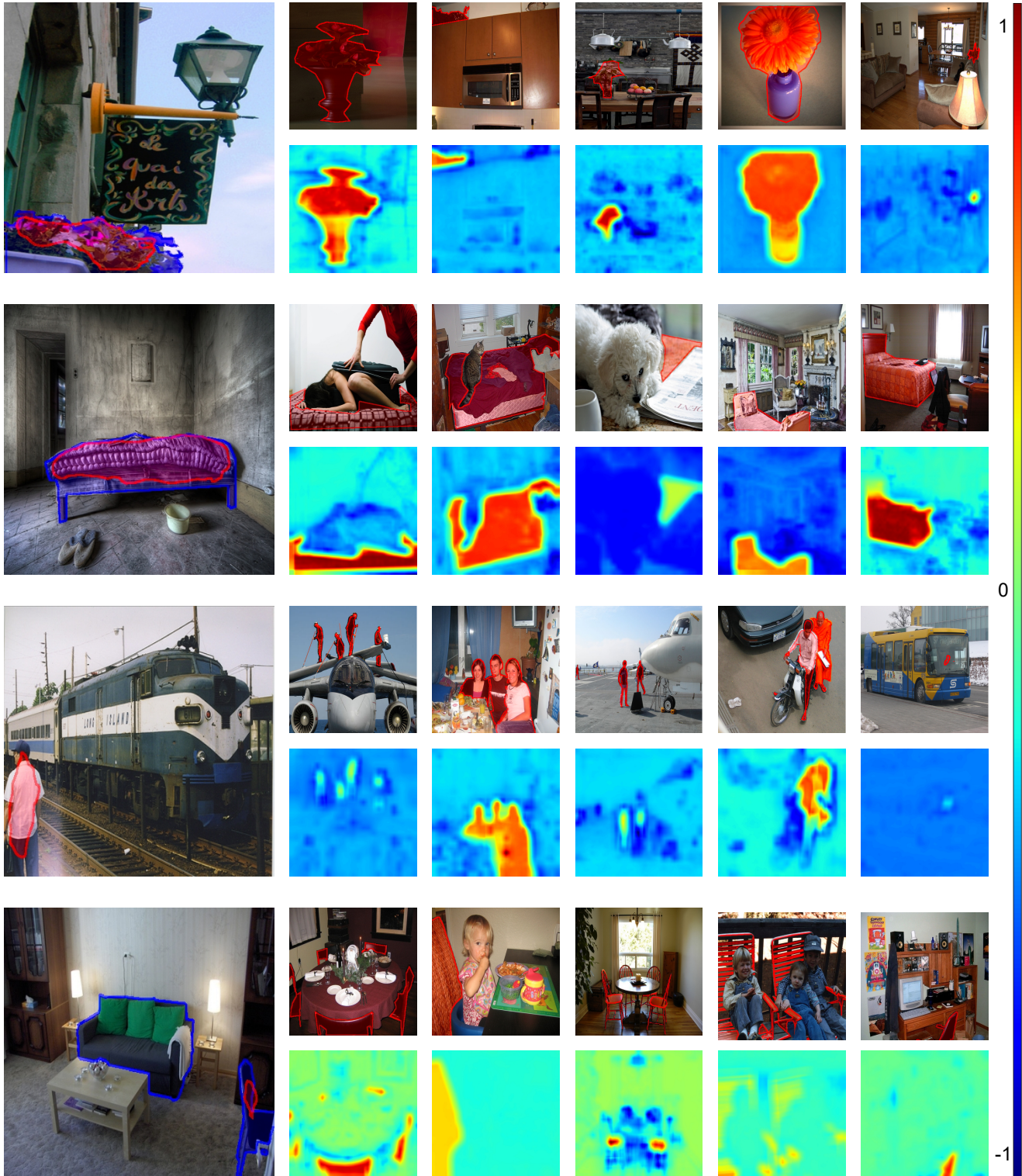


Figure S.3. Qualitative results for Signed AffEx with DCAMA across multiple episodes from COCO-20ⁱ (first two rows) and Pascal-5ⁱ (last two rows). For each episode, the left column shows the query image with the predicted segmentation in red; the ground truth is overlaid in blue when it significantly differs from the prediction. The right column presents the corresponding support set alongside the attribution maps produced by the proposed method.

rise, accompanied by fluctuations in the confidence maps. As this episode is more challenging, the model requires a larger fraction of inserted pixels to achieve a satisfactory segmentation, leading to a less pronounced IAUC slope. Conversely, removing only 20% of the most important pixels already reduces the score below 0.2, producing a steep DAUC curve. Unlike the first episode, the confidence maps in the early DAUC steps immediately deteriorate, and the model begins to highlight and segment different, inconsistent regions.

Together, these examples demonstrate how IAUC and DAUC can vary substantially depending on episode difficulty and the model’s reliance on particular support pixels, underscoring the relevance of these metrics for evaluating interpretability methods, while also highlighting their limitations when used in isolation.

S.6. Future Works

Beyond the future directions discussed in the main paper, we identify additional promising avenues for extension. Our current approach relies on the approximation $\alpha_{i,x,y} \approx \mathcal{A}(F_{\theta_q}, (u, v), F_{\theta_S}) \approx \mathcal{A}(P_q, (u, v), P_S)$, which effectively disregards the interpretability contributions of the feature extractor. A natural next step is to incorporate complementary XAI techniques—such as Grad-CAM [31] applied directly to the feature extractor—to capture these contributions more faithfully and combine them with AffEx’s attribution maps. Such a hybrid approach could provide more comprehensive explanations by accounting for both the feature extraction and relational reasoning stages of FSS models, while also increasing the spatial resolution and detail of the resulting attributions.

Another promising direction is to extend our method to prototype-based FSS models [5, 7, 46, 50, 54], which do not explicitly compute similarity maps between query and support features. These models are not *interpretable by design*, but prototype similarities could be combined with attribution methods to trace which support regions most influence the prototype representations and, consequently, the final predictions. This extension would broaden AffEx’s applicability to a broader range of FSS architectures, enhancing its utility across diverse scenarios.

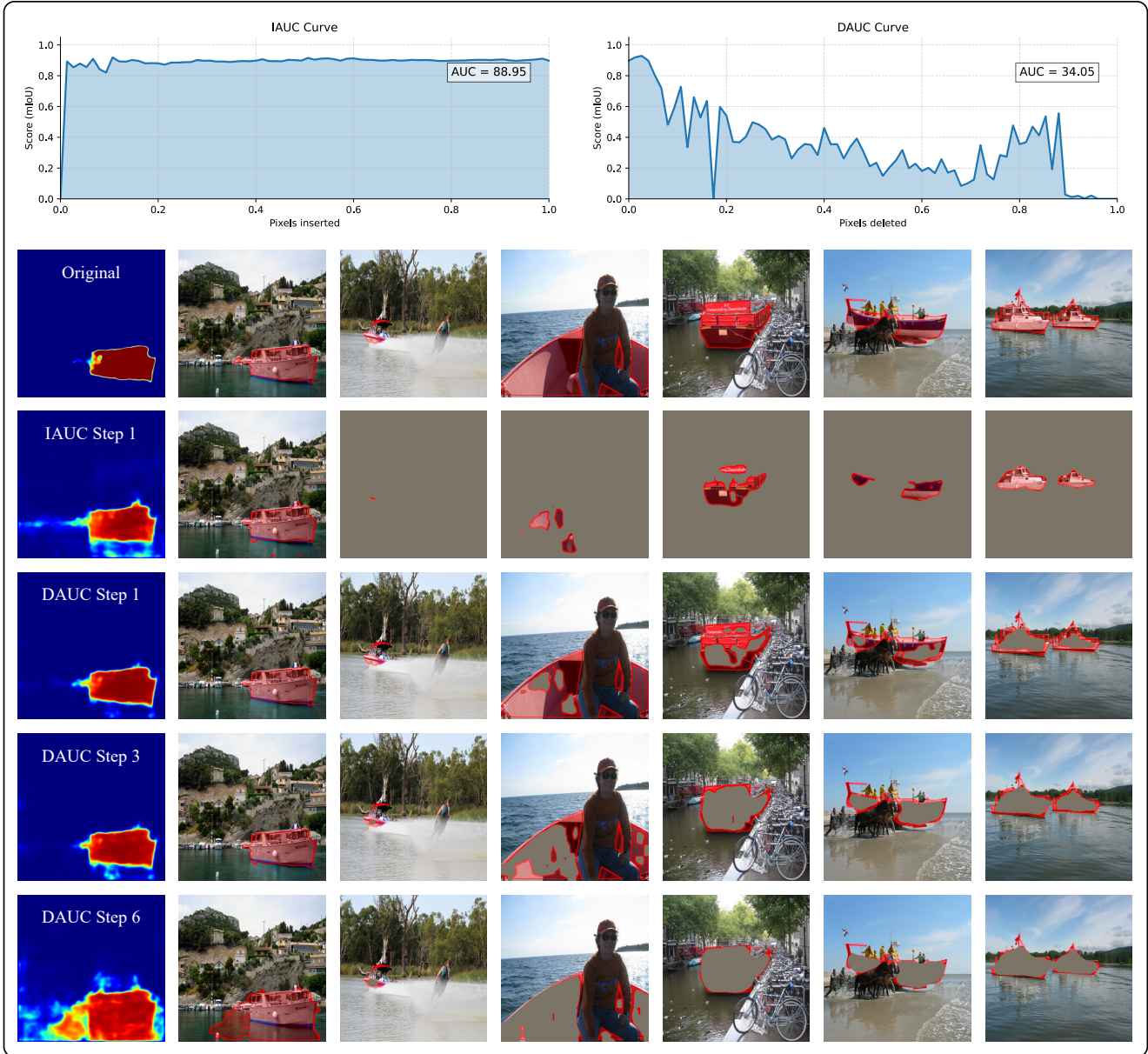


Figure S.4. A visually clean episode of the insertion and deletion evaluation for DCAMA on COCO-20ⁱ using Signed AffEx. The top row reports the IAUC and DAUC curves for a case with a clearly delineated foreground object. Subsequent rows show the confidence map, the predicted query mask (red) overlaid with the ground truth (blue), and the support images with their masks at different insertion/deletion steps, illustrating stable attribution behavior.

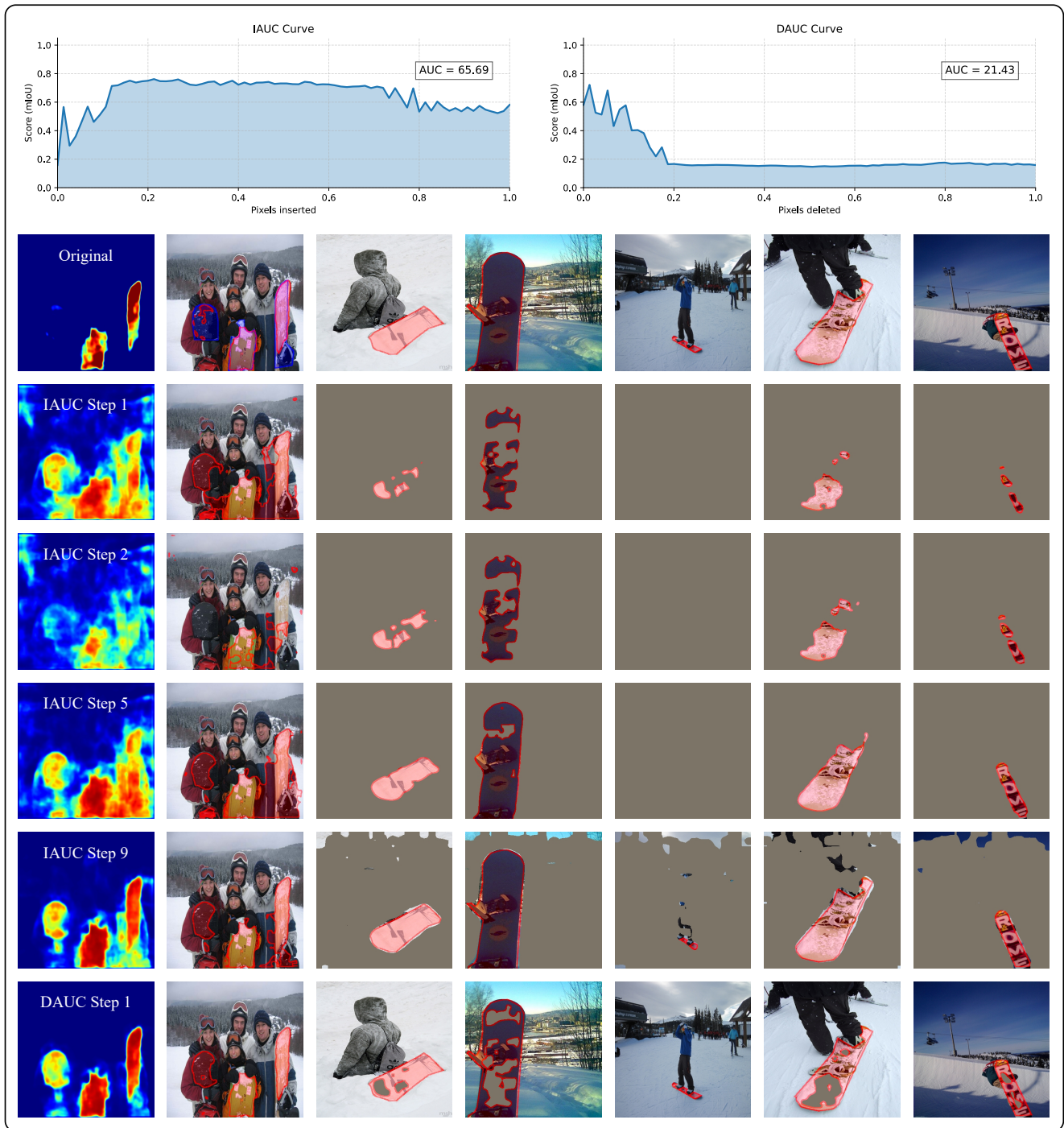


Figure S.5. A challenging episode highlighting unstable insertion and deletion behavior for DCAMA on COCO-20ⁱ with Signed AffEx. The top row presents IAUC and DAUC curves reflecting the increased difficulty of this scenario. The lower rows display the confidence map, the predicted query mask (red) against the ground truth (blue), and the support images with their masks across insertion/deletion steps, revealing fluctuations in evidence attribution.